An inherent-optical-property-centered approach to correct the angular effects in water-leaving radiance

Zhong Ping Lee,[1,*] Keping Du,[2] Kenneth J. Voss,[3] Giuseppe Zibordi,[4] Bertrand Lubac,[5] Robert Arnone,[6] and Alan Weidemann[6]

[1]Geosystems Research Institute, Mississippi State University, Stennis Space Center, Mississippi 39529, USA

[2]State Key Laboratory of Remote Sensing Science, Research Center for Remote Sensing and GIS, School of Geography, Beijing Normal University, Beijing, 100875, China

[3]Department of Physics, University of Miami, Coral Gables, Florida 33124, USA

[4]Global Environment Monitoring Unit, Joint Research Center, 21027 Ispra, Italy

[5]UMR-EPOC 5805, CNRS, Université de Bordeaux 1, Talence, 33405, France

[6]Naval Research Laboratory, Stennis Space Center, Mississippi 39529, USA

*Corresponding author: zplee@ngi.msstate.edu

Received 12 January 2011; revised 29 March 2011; accepted 6 April 2011; posted 19 April 2011 (Doc. ID 141059); published 22 June 2011

Remote-sensing reflectance (R_{rs}), which is defined as the ratio of water-leaving radiance (L_w) to downwelling irradiance just above the surface ($E_d(0^+)$), varies with both water constituents (including bottom properties of optically-shallow waters) and angular geometry. L_w is commonly measured in the field or by satellite sensors at convenient angles, while $E_d(0^+)$ can be measured in the field or estimated based on atmospheric properties. To isolate the variations of R_{rs} (or L_w) resulting from a change of water constituents, the angular effects of R_{rs} (or L_w) need to be removed. This is also a necessity for the calibration and validation of satellite ocean color measurements. To reach this objective, for optically-deep waters where bottom contribution is negligible, we present a system centered on water's inherent optical properties (IOPs). It can be used to derive IOPs from angular R_{rs} and offers an alternative to the system centered on the concentration of chlorophyll. This system is applicable to oceanic and coastal waters as well as to multiband and hyperspectral sensors. This IOP-centered system is applied to both numerically simulated data and *in situ* measurements to test and evaluate its performance. The good results obtained suggest that the system can be applied to angular R_{rs} to retrieve IOPs and to remove the angular variation of R_{rs}.

OCIS codes: 010.4450, 010.0280.

1. Introduction

Water-leaving radiance (L_w, $W\,m^{-2}\,sr^{-1}$. See Table 1 for primary symbols used in this article) is the light intensity per solid angle resulting from absorption and scattering processing in the water. Spectral L_w provides key information to remotely sense water constituents in the upper water column, as it varies, both in magnitude and spectral shape, with changing concentrations of optically significant constituents and bottom properties (bottom depth and bottom reflectivity) if the sea bottom is optically shallow. Accurate determination of L_w, from *in situ* or satellite sensors, is a fundamental goal for ocean color satellite missions.

L_w varies not only with wavelength (λ, nm) and water constituents but also with angular geometry: θ_S, θ_v, φ (collectively represented as Ω in the following text unless further clarification is needed). Here, θ_S is the solar zenith angle in air (θ_v, φ), determines

0003-6935/11/193155-13$15.00/0

Table 1. Notation

Symbol	Definition or Description	Units
a	Absorption coefficient	m^{-1}
b	Scattering coefficient	m^{-1}
b_b	Backscattering coefficient ($= b_{bw} + b_{bp}$)	m^{-1}
b_{bw}, b_{bp}	Backscattering coefficient of water molecules and particles, respectively	m^{-1}
b_f	Forward scattering coefficient	m^{-1}
c	Beam attenuation coefficient ($= a + b$)	m^{-1}
D_d	Distribution function of downwelling irradiance	-
E_d	Downwelling irradiance	$W\,m^{-2}$
E_{od}	Downwelling scalar irradiance	$W\,m^{-2}$
E_{ou}	Upwelling scalar irradiance	$W\,m^{-2}$
f	Model coefficient for subsurface irradiance reflectance	-
g	Model coefficients for subsurface remote sensing reflectance	sr^{-1}
G	Model coefficients for above-surface remote sensing reflectance	sr^{-1}
k_L	Attenuation coefficient of upwelling radiance	m^{-1}
L	Radiance	$W\,m^{-2}\,sr^{-1}$
L_u	Upwelling radiance	$W\,m^{-2}\,sr^{-1}$
L_w	Water-leaving radiance	$W\,m^{-2}\,sr^{-1}$
$[L_w]_N$	Normalized water-leaving radiance	$W\,m^{-2}\,sr^{-1}$
n	Refractive index of water	-
Q	Ratio of irradiance to radiance	sr
r_{rs}	Subsurface remote sensing reflectance ($= L_u(0^-)/E_d(0^-)$)	sr^{-1}
R_{rs}	Above-surface remote-sensing reflectance ($= L_w(0^+)/E_d(0^+)$)	sr^{-1}
β	Volume scattering function	$m^{-1}\,sr^{-1}$
κ	Quasi-diffuse attenuation coefficient ($= a + b_b$)	m^{-1}
λ	Wavelength	nm
θ_S	Solar zenith angle in air	rad
θ_v	Sensor nadir-view angle in air	rad
φ	Sensor azimuth angle in relation to the solar plane	rad
Ω	Collectively representing sun-sensor angular geometry ($\theta_S, \theta_v, \varphi$)	rad
ρ	Fresnel reflectance	-
$\Re$	Divergence factor when radiance enters into air from below the surface	-

the angular direction of L_w with θ_v the zenith angle of the radiance (= sensor's view angle from nadir) in air, and φ the azimuth angle relative to the sun plane. Figure 1 presents the angular coordinates used in this article. For Ω defined by $\theta_S = 30°$, $\theta_v = 30°$ and $\varphi = 180°$, L_w is in a direction going to the sun (the sensor has its back face towards the sun and measures more backscattered photons from the sun beam); while for an Ω with $\theta_S = 30°$, $\theta_v = 30°$, and $\varphi = 0°$, L_w is in a direction going further away from the sun (and a remote sensor would measure the specular reflection of the solar light from air-sea interface).

Because $L_w(\lambda, \Omega)$ varies with Ω for the same water constituents under the same solar illumination [1], it is necessary to remove/correct this angular variation (also called the bidirectional reflectance distribution function [BRDF]) in order to isolate the constituent-caused, versus geometric (different time or different location) variation of $L_w(\lambda, \Omega)$. This is also important/

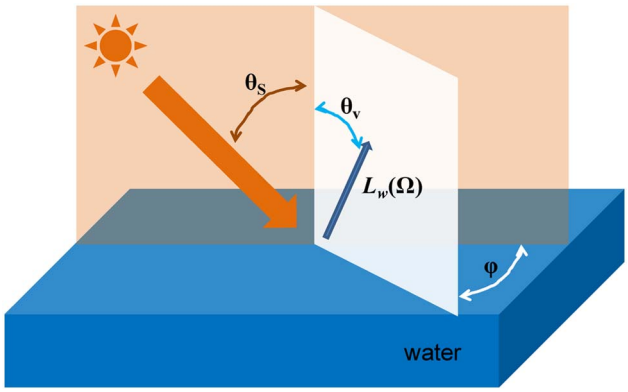

Fig. 1. (Color online) Angular coordinate used in this study and the IOP-centered system.

required for the vicarious calibration of space sensors and the validation of $L_w(\lambda, \Omega)$ derived from different sensors which have different measurement geometries. Because of this demand, the concept of normalized water-leaving radiance $[L_w(\lambda)]_N$ was introduced [2–4]. This quantity is a hypothetical value of L_w with zenith angle of 0° (sensor looking vertically down, $\theta_v = 0°$), the sun at zenith ($\theta_S = 0°$), and a black sky (no atmosphere between the sun and the water). Changes in $[L_w(\lambda)]_N$ at different locations and times thus represent only changes of water constituents. Because the actually measured property is $L_w(\lambda, \Omega)$, a method to convert $L_w(\lambda, \Omega)$ to $[L_w(\lambda)]_N$ is required.

In the 1990s, for optically deep waters, Morel *et al.* [1,4,5] developed a conversion system for optically deep waters based on the Case 1 assumption [6], which uses concentration of chlorophyll (Chl) as an input for calculations. To briefly summarize, a relationship between $[L_w(\lambda)]_N$ and $L_w(\lambda, \Omega)$ is expressed as

$$\frac{[L_w(\lambda)]_N}{L_w(\lambda, \Omega)} = \frac{F_0(\lambda)}{E_d(0^+, \lambda, \theta_S)} \frac{[\Re]_N}{\Re(\theta_S, \theta_v)} \frac{[f(\lambda)]_N}{[Q(\lambda)]_N} \frac{Q(\lambda, \Omega)}{f(\lambda, \theta_S)}. \quad (1)$$

Here, F_0 ($W\,m^{-2}$) is the solar irradiance at the top of the atmosphere and for the mean sun-earth distance, and E_d is the spectral downwelling irradiance just above the surface when L_w is measured. Parameter $\Re$ represents cross-surface effects [5,7] when upwelling radiance enters into air from the water; f relates subsurface irradiance reflectance with the ratio of backscattering coefficient (b_b, m^{-1}) to absorption coefficient (a, m^{-1}) [8]; and Q represents the ratio of subsurface upwelling irradiance to subsurface upwelling radiance [1] corresponding to $L_w(\lambda, \Omega)$. Consistently, $[f(\lambda)]_N$ and $[Q(\lambda)]_N$ indicate the values of $f(\lambda, \theta_S)$ and $Q(\lambda, \Omega)$ corresponding to $[L_w(\lambda)]_N$.

In Eq. (1), F_0 is known, E_d can be calculated based on known atmosphere information [9], variation of $\Re$ can be determined based on information of angular geometry and is found nearly independent of wind speed [7]. The remaining unknowns are f and Q as

they vary with wavelength, angular geometry, and water constituents. Based on the Case 1 assumption [10,11], where the water's spectral optical properties can be determined by the concentration of Chl alone [12], variations of both f and Q (and their ratios) have been developed [5] and validated [13] for a set of Chl values and wavelengths. Consequently, when Chl is known or estimated from measured $L_w(\lambda,\Omega)$, $[L_w(\lambda)]_N$ can then be determined based on Eq. (1).

This system requires knowledge of the concentration of Chl and works only with Case 1 waters [1,5,14], thus its application excludes waters that do not fall into the Case 1 category, which includes many coastal as well as oceanic waters [15]. The following details an alternative approach that uses the water's inherent optical properties (IOPs) as inputs for calculations and does not require the Case 1 assumption, thus it could be applied to both oceanic waters and coastal waters. The performance of this approach to both numerically simulated data and field measured data is also presented. Because bottom reflectance may significantly modify the BRDF of $L_w(\lambda,\Omega)$ [16], the study here is focused on optically-deep waters. In addition, the contribution to $L_w(\lambda,\Omega)$ resulted from inelastic scattering (like Raman scattering [17,18] or chlorophyll-a fluorescence whose angular distribution is isotropic [19]) is not included.

2. Theoretical Basis

The subsurface remote-sensing reflectance (r_{rs}, sr^{-1}) is defined as

$$r_{rs}(\lambda,\Omega') = \frac{L_u(0^-,\lambda,\Omega')}{E_d(0^-,\lambda,\theta'_S)}, \tag{2}$$

where $L_u(0^-,\lambda,\Omega')$ is the subsurface upwelling radiance and $E_d(0^-,\lambda,\theta'_S)$ is the subsurface downwelling irradiance (θ'_S is the in-water zenith angle of θ_S). $L_w(\lambda,\Omega)$ can then be expressed as [20]

$$L_w(\lambda,\Omega) = \frac{1-\rho(\theta'_v,\varphi)}{n^2} E_d(0^-,\lambda,\theta'_S) r_{rs}(\lambda,\Omega'), \tag{3}$$

where ρ is the Fresnel reflectance corresponding to θ'_v (in-water zenith angle of θ_v), and n is the refractive index of water. This relationship indicates that the angular variation of $L_w(\lambda,\Omega)$ is mainly determined by the angular shape of $r_{rs}(\lambda,\Omega')$.

Based on the radiative transfer theory, Zaneveld [21,22] has shown that $r_{rs}(\lambda,\Omega')$ of optically-deep waters is

$$r_{rs}(\lambda,\Omega') \equiv \frac{D_d(\lambda,\theta'_S)}{c(\lambda)+k_L(\lambda,\Omega')-f_L(\lambda,\Omega')b_f(\lambda)} \times \frac{\int_0^{2\pi}\int_0^{\pi/2}\beta(\Omega',\Omega)L(\lambda,\Omega')\sin(\theta')\mathrm{d}\theta'\mathrm{d}\varphi'}{E_{od}(0^-,\lambda,\theta'_S)}. \tag{4}$$

Here, D_d is the distribution function for the downwelling light [23], c (m^{-1}) is the beam attenuation coefficient, k_L (m^{-1}) is the diffuse attenuation coefficient for upwelling radiance [22], f_L is the shape parameter for radiance [22], b_f (m^{-1}) is the forward scattering coefficient, β ($m^{-1}\,sr^{-1}$) is the volume scattering function (VSF) of the water media, L is radiance at an angle (θ',ϕ'), and E_{od} is the downwelling scalar irradiance. In essence, r_{rs} depends on the water IOPs and the radiance-sun angular geometry [1,22,24].

Under the quasi-single scattering assumption [25], Eq. (4) for zenith-going radiance ($L_u(0^-,\lambda,0°)$) can be simplified as [26,27]

$$r_{rs}(\lambda,0°) = \frac{D_d(\lambda,\theta'_S)\beta(180-\theta'_S)}{a(\lambda)+k_L(\lambda,0°)}. \tag{5}$$

This formulation, although with larger errors resulting from the omission of multiple scattering, highlights that $r_{rs}(\lambda,\Omega')$ is fundamentally dependent on the optical properties [5,24] (e.g., absorption and backscattering coefficients) and the angular shape of the VSF (or phase function) [27,28]. Consequently, it is necessary to know both in order to accurately remove the angular variation of $r_{rs}(\lambda,\Omega')$ or $L_w(\lambda,\Omega)$, especially for wavelengths where single scattering dominates.

Unfortunately, in ocean color remote sensing, the only available information is $L_w(\lambda,\Omega)$ (when boundary conditions are adequately known), therefore the optical properties of the water must be derived first from $L_w(\lambda,\Omega)$ in order to achieve the BRDF correction. While the angular shape of β is composed of both water molecule and particle scattering, it has been found that the angular shape of the particle scattering phase function is not a constant and varies with particle size and composition [29–31]. To extend the dilemma further: at present, there is no reliable method yet to accurately estimate the particle phase function shape from remote-sensing measurements. As a result, in ocean color remote sensing, a phase function (or phase functions [5]) for particle scattering has to be assumed in order to develop an analytical model [1,23,24,32] to process remotely sensed data. Fortunately, the variation of particle phase function of global waters is within limited ranges [31]. The fact that particle phase functions do vary indicates that the BRDF correction in ocean color remote sensing will always be a best-effort estimate, unless multiple scattering has created a completely diffuse upwelling light field.

As discussed above, even after we assume that the particle scattering phase function is known, it is still required to know the optical properties (e.g., absorption and diffuse attenuation coefficients) for the correction of angular effects. Because the diffuse attenuation coefficients are mainly determined by the absorption (a) and backscattering (b_b) coefficients [33–35], thus the logical focus is to derive a and b_b from the measured $L_w(\lambda,\Omega)$. This could not be achieved through Eq. (4) as it is not directly invertible. To expedite the inversion process, numerous attempts have been made to obtain a simplified,

but sufficiently accurate, analytical formulation to describe $r_{rs}(\lambda,\Omega')$.

3. Model for Remote-Sensing Reflectance

In the past decades, following various numerical simulations, a series of formulas have been developed to achieve a simplified expression for Eq. (4). These include the pioneer polynomial model developed by Gordon *et al.* [24] for nadir-viewed r_{rs}:

$$r_{rs}(\lambda,\theta_v=0^\circ)=\left[g_0+g_1\left(\frac{b_b(\lambda)}{a(\lambda)+b_b(\lambda)}\right)\right]\frac{b_b(\lambda)}{a(\lambda)+b_b(\lambda)}. \tag{6}$$

Albert and Mobley [36] expanded the above to a 4th-order polynomial, with coefficients developed for various angles and wind speed (w, $\mathrm{m\,s^{-1}}$):

$$r_{rs}(\lambda,\Omega')=q(\Omega',w)\sum_{i=1}^{4}p_i\left(\frac{b_b(\lambda)}{a(\lambda)+b_b(\lambda)}\right)^i. \tag{7}$$

To explicitly account for the effects of molecular and particle scatterings [37], Lee *et al.* [38,39] proposed a two-term formula to model $r_{rs}(\lambda,\Omega')$:

$$r_{rs}(\lambda,\Omega')=g_w(\Omega')\frac{b_{bw}(\lambda)}{a(\lambda)+b_b(\lambda)}+g_p(\lambda,\Omega')\frac{b_{bp}(\lambda)}{a(\lambda)+b_b(\lambda)}. \tag{8}$$

Separately, Park and Ruddick [40] used a 4th-order polynomial with model coefficients as functions of the relative contributions (v_b) of molecular scattering to the total scattering:

$$r_{rs}(\lambda,\Omega')=\sum_{i=1}^{4}g_i(\Omega',\nu_b)\left(\frac{b_b(\lambda)}{a(\lambda)+b_b(\lambda)}\right)^i. \tag{9}$$

Lately, Van Der Woerd and Pasterkamp [41] proposed a significantly different polynomial form

$$\ln[r_{rs}(\lambda,\Omega')]=\sum_{i=1}^{4}\sum_{j=1}^{4}P_{ij}(\Omega')[\ln(a(\lambda))]^i[\ln(b(\lambda))]^j. \tag{10}$$

These models, although not exhaustive of those in the literature, all used the particle phase function measured by Petzold [29] and in general produce consistent r_{rs} for given IOPs. They do, however, have subtle differences in complexity and representation of radiative transfer.

Because a remote sensor measures $L_w(\lambda,\Omega)$ instead of $L_u(0^-,\lambda,\Omega')$, we take a slightly different approach in the modeling step. Defining the remote-sensing reflectance (R_{rs}) as the ratio of $L_w(\lambda,\Omega)$ to $E_d(0^+,\lambda,\theta_S)$:

$$R_{rs}(\lambda,\Omega)=\frac{L_w(\lambda,\Omega)}{E_d(0^+,\lambda,\theta_S)}. \tag{11}$$

For an easier description and following the approach of Gordon *et al.* [24], R_{rs} of optically deep waters is considered as a generic function of a model parameter (G) and water's IOPs:

$$R_{rs}(\lambda,\Omega)=G(\lambda,\Omega)\mathrm{Fun}(\mathrm{IOP}(\lambda)). \tag{12}$$

Here the angular variation of R_{rs} is represented by G, which may also vary with IOPs as shown for subsurface remote-sensing reflectance (see Eq. (6)). The remote-sensing reflectance corresponding to $[L_w]_N$ is

$$[R_{rs}(\lambda)]_N=[G(\lambda)]_N\mathrm{Fun}(\mathrm{IOP}(\lambda)), \tag{13}$$

and $[L_w(\lambda)]_N$ will simply be the product of $[R_{rs}(\lambda)]_N$ and $F_0(\lambda)$. The challenge of the BRDF correction then becomes how to convert $G(\lambda,\Omega)$ to $[G(\lambda)]_N$ when $R_{rs}(\lambda,\Omega)$ is the only known, where as $G(\lambda,\Omega)$ may also vary with IOPs (see Eqs. (6)–(9)).

With an objective to efficiently process a large volume of satellite data, and at the same time explicitly reveal the different effects of molecular scattering versus particle scattering [37,39], we selected a formula similar as Eq. (8) to model $R_{rs}(\lambda,\Omega)$:

$$R_{rs}(\lambda,\Omega)=\left(G_0^w(\Omega)+G_1^w(\Omega)\frac{b_{bw}(\lambda)}{\kappa(\lambda)}\right)\frac{b_{bw}(\lambda)}{\kappa(\lambda)}+\left(G_0^p(\Omega)+G_1^p(\Omega)\frac{b_{bp}(\lambda)}{\kappa(\lambda)}\right)\frac{b_{bp}(\lambda)}{\kappa(\lambda)}, \tag{14}$$

with $\kappa\equiv a+b_b$. This formulation integrates the cross-surface effects ($\Re(\theta_S,\theta_v)$) and the expression for r_{rs} into one equation, simply to expedite data processing. This is also because the value of $\Re(\theta_S,\theta_v)$ can be well determined based on angular geometry and it is nearly independent of the wind speed [7]. Expressions for $R_{rs}(\lambda,\Omega)$ with explicitly separated $\Re(\theta_S,\theta_v)$ and r_{rs}, however, are also available.

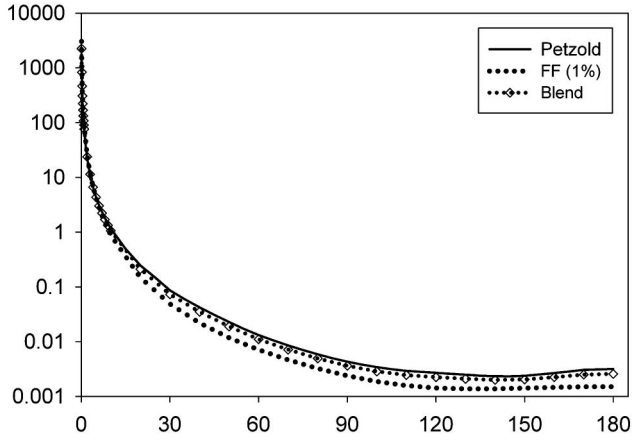

Fig. 2. Particle phased function shapes (Petzold average and 1% Fournier and Forand) used for the numerical simulation. The open diamond represents one weighted average of the particle assemblage.

Table 2. Sample Values of ($G_0^w(\Omega)$, $G_1^w(\Omega)$, $G_0^p(\Omega)$, $G_1^p(\Omega)$) for Angular R_{rs}

$\theta_S \Rightarrow$	0°	0°	15°	30°	0°	15°	30°
$\theta_v \Rightarrow$	0°	30°	30°	30°	40°	40°	40°
$\varphi \Rightarrow$	0°	90°	90°	90°	135°	135°	135°
G_w^0	0.0604	0.0596	0.0590	0.0584	0.0581	0.0614	0.0624
G_w^1	0.0406	0.0516	0.0562	0.0601	0.0581	0.0524	0.0524
G_p^0	0.0402	0.0408	0.0411	0.0418	0.0414	0.0425	0.0434
G_p^1	0.1310	0.1420	0.1461	0.1492	0.1458	0.1408	0.1406

The model coefficients ($G_0^w(\Omega)$, $G_1^w(\Omega)$, $G_0^p(\Omega)$, and $G_1^p(\Omega)$) in Eq. (14) are now dependent on angular geometry and phase function, but independent of absorption and backscattering coefficients or wavelength. Similarly to earlier studies [8,23,32,42], the values of ($G_0^w(\Omega)$, $G_1^w(\Omega)$, $G_0^p(\Omega)$, and $G_1^p(\Omega)$) were derived with numerically simulated remote-sensing reflectance and with preselected particle phase functions.

We took advantage of the synthetic dataset included in the IOCCG Report #5 [43], where 500 sets of spectral IOPs are available ($b_b/(a+b_b)$: 0.0002–0.37) in a spectral range from 400 to 800 nm (resolution is 10 nm). Two particle phase functions were used for the simulation, one for mineral like particles and the other for phytoplankton, to better represent the collective particle scattering of an assemblage of particles. The former is represented with the Petzold average [20], while the latter is represented by a particle phase function with a backscattering-to-scattering ratio as 1% [44]. Figure 2 presents the Petzold average, the 1% Fournier–Forand phase function, and an example of the blended phase functions. The simulation (by Hydrolight [45]) in the IOCCG Report #5 [43] covered only two sun angles (30° and 60°); here, we extended that to cover sun angles from 0 to 75°.

For θ_S from 0 to 75° (resolution is 15°), θ_v from 0 to 70° (resolution is 10°), and φ from 0 to 180° (resolution is 15°), a total ($6 \times 7 \times 13 + 6$) set of constants representing ($G_0^w(\Omega)$, $G_1^w(\Omega)$, $G_0^p(\Omega)$, and $G_1^p(\Omega)$) were derived (by least-square fit) from the simulated $R_{rs}(\lambda, \Omega)$. Table 2 provides a few samples of the model coefficients. Note that these values can be easily revised/updated when a more suitable phase function (s) is accepted by the community.

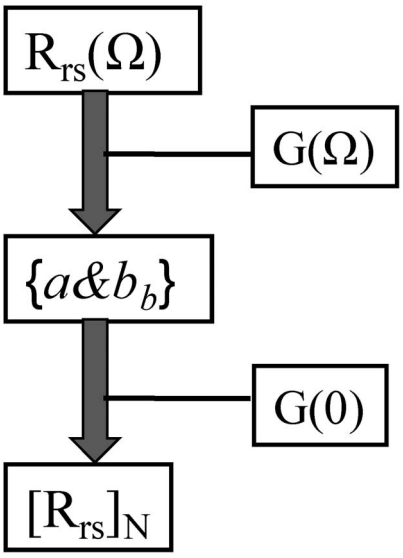

Fig. 3. Schematic data flow chart of the IOP-centered BRDF correction scheme.

4. Retrieve of IOPs from Angular R_{rs} and the BRDF Correction

As discussed in Section 3 and based on Eq. (14), the absorption and backscattering coefficients are required in order to obtain $[R_{rs}]_N$. Figure 3 shows a general data flow chart of the IOP-based BRDF correction scheme. We here take the quasi-analytical algorithm (QAA) strategy [46,47] for the derivation of the IOPs from $R_{rs}(\lambda, \Omega)$. This is because in the QAA system, the $R_{rs}(\lambda, \Omega)$ modeled with the derived a and b_b represents exactly the measured $R_{rs}(\lambda, \Omega)$. On the other hand, if a spectral optimization approach [48–50] is used for the derivation of a and b_b, the modeled $R_{rs}(\lambda, \Omega)$ with the derived a and b_b does not match the measured $R_{rs}(\lambda, \Omega)$ exactly. This difference in $R_{rs}(\lambda, \Omega)$ will result in extra uncertainty in the estimated $[R_{rs}(\lambda)]_N$ when the optimization-derived a and b_b is applied.

In the QAA, absorption at a reference wavelength λ_0, $a(\lambda_0)$, is estimated first, and then particle backscattering at this wavelength ($b_{bp}(\lambda_0)$). $a(\lambda)$ is then derived analytically from $R_{rs}(\lambda, \Omega)$ after propagating this $b_{bp}(\lambda_0)$ to $b_{bp}(\lambda)$ with a power-law model [10,46]. These derived $a(\lambda)$ and $b_{bp}(\lambda)$ are introduced into Eq. (14), and applying the ($G_0^w(\Omega)$, $G_1^w(\Omega)$, $G_0^p(\Omega)$, and $G_1^p(\Omega)$) values for the angular geometry $(0°, 0°, 0°)$ of normalized water-leaving radiance to determine $[R_{rs}(\lambda)]_N$.

In the derivation process, λ_0 is selected as 550, 555, or 560 nm for Moderate Resolution Imaging Spectroradiometer (MODIS), Sea-viewing Wide Field-of-view Sensor (SeaWiFS), and MEdium Resolution Imaging Spectrometer (MERIS) sensors, respectively, and $a(\lambda_0)$ is estimated from (QAA-v5, http://www.ioccg.org/groups/Software_OCA/QAA_v5.pdf)

$$\begin{cases} \chi = \log\left(\dfrac{R_{rs}(443)+R_{rs}(490)}{R_{rs}(\lambda_0)+5\frac{R_{rs}(667)}{R_{rs}(490)}R_{rs}(667)}\right), \\ a(\lambda_0) = a_w(\lambda_0) + 10^{-1.146-1.366\chi-0.469\chi^2}. \end{cases} \quad (15)$$

The coefficients in Eq. (15) are averages for those sensors, but individual coefficients for each sensor are available. Because the variation of the spectral

ratio of $R_{rs}(\lambda,\Omega)$ for different Ω is quite limited, the constants in Eq. (15) are used for R_{rs} of all Ω. Impact of the error of $a(\lambda_0)$ on the BRDF correction is presented in Subsection 5.B.3.

When $a(\lambda_0)$ is known, Eq. (14) becomes a quadratic function of $b_{bp}(\lambda_0)$:

$$Ax^2 + Bx + C = 0, \tag{16}$$

with $x = b_{bp}(\lambda_0)$ and

$$\begin{cases} A = G_0^p + G_1^p - R_{rs}, \\ B = G_0^w b_{bw} + G_0^p(a + b_{bw}) - 2R_{rs}(a + b_{bw}), \\ C = G_0^w b_{bw}(a + b_{bw}) - R_{rs}(a + b_{bw})^2 + G_1^w (b_{bw})^2. \end{cases} \tag{17}$$

$b_{bp}(\lambda_0)$ is then derived by solving Eq. (16). Note that the R_{rs}, a, and b_{bw} in Eq. (17) are values at λ_0. $b_{bp}(\lambda)$ is further derived with a power-law function [10] where the exponent is estimated empirically [46] (also see http://www.ioccg.org/groups/Software_OCA/QAA_v5.pdf).

When $b_{bp}(\lambda)$ is known, Eq. (14) becomes a quadratic equation of κ:

$$R_{rs}\kappa^2 - X\kappa - Y = 0, \tag{18}$$

with

$$\begin{cases} X = G_0^w b_{bw} + G_0^p b_{bp}, \\ Y = G_1^w (b_{bw})^2 + G_1^p (b_{bp})^2. \end{cases} \tag{19}$$

And

$$a = \kappa - b_{bw} - b_{bp}, \tag{20}$$

after κ is derived by solving Eq. (18). R_{rs}, b_{bw}, b_{bp}, and κ in Eqs. (18)–(20) are values at λ.

5. Validation of the IOP-Based BRDF Correction Scheme

The IOP-based BRDF correction scheme is applied to both numerically simulated and field measured data to evaluate its performance.

A. Data Simulated with Hydrolight

For a self-consistency check, the above BRDF correction scheme was first applied to a subset of data simulated by Hydrolight (Section 3). We focused on L_w with the sun at 60° from zenith, and the sensor viewing angle in a range of 30–70° and azimuth angles of 0–180°, an angular domain which shows a large difference between $L_w(\lambda,0°)$ (nadir-measured L_w) and $L_w(\lambda,\Omega)$. Here, we compared $L_w(\lambda,\Omega)$ with $L_w(\lambda,0°)$ (i.e., if there is no correction at all), and compared them between $L_w(\lambda,\Omega)$-generated $L_w(\lambda,0°)$ with $L_w(\lambda,0°)$ (i.e., after a BRDF correction). For each pair of L_w, an absolute difference is calculated as

$$\delta = \frac{|L - L_w(\lambda,0°)|}{L_w(\lambda,0°)} \times 100. \tag{21}$$

Here, L represents either $L_w(\lambda,\Omega)$ (before correction) or $L_w(\lambda,\Omega)$-generated $L_w(\lambda,0°)$ (i.e., after correction). The distribution of δ is shown in Fig. 4.

It is found that without a BRDF correction, only 23.7% of the dataset have δ within 5%, and more than 50% of the data have $\delta > 10\%$, which is consistent with results shown in earlier studies [1,5]. After applying the IOP-based BRDF correction scheme, however, 92.3% of the data have δ within 5%, and only 1.4% of the data have $\delta > 10\%$. These results demonstrate that the IOP-based BRDF correction scheme (which is composed of the R_{rs} model along with the IOP retrieval algorithm) works very well with the numerically simulated data. This could be in part because the model and dataset have the same particle phase functions.

B. Field Measured Data

1. *Comparison of NuRADS Measurements*

The upwelling radiance distribution was measured using two systems. For the AOPEX dataset (experiments in the Mediterranean Sea, August 2004), NuRADS [51] were used. For the Monterey Bay experiment, a combination of the NuRADS systems were used, which also allowed measurement of the polarized radiance distribution [52]. The NuRADS systems measure the in-water upwelling spectral radiance distribution and are based on a fisheye camera system and an electronic camera. With these systems, the entire hemispherical radiance distribution can be measured, at one wavelength, in a single image [51].

For the data used in this paper, the upwelling radiance distribution was averaged over 10 min

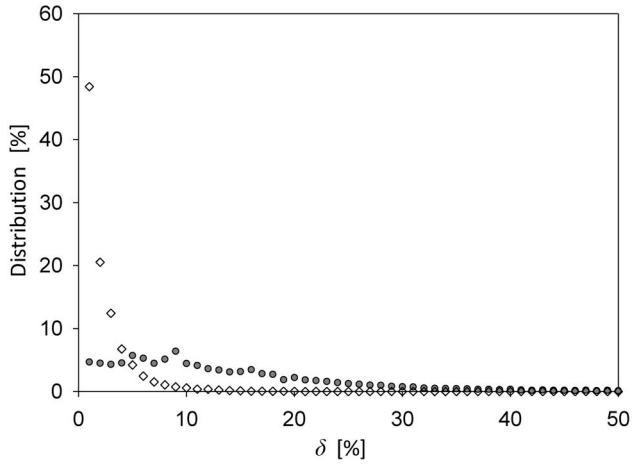

Fig. 4. Distribution of absolute percentage difference (δ) of L_w. Simulated data were used, and focused on the angular domain that $\theta_S = 60°$, $\theta_v = 30°$–$70°$, and $\varphi = 0°$–$180°$. Solid circle, no BRDF correction; open diamond, after IOP-based BRDF correction.

periods. Each NuRADS image takes on the order of 0.1 s to acquire; however, because of the time required to rotate through the spectral bands and store the data, there are approximately five images at each wavelength which can be averaged in the 10 min period.

While $L_u(\lambda,\Omega)$ is measured in radiometric units, because of the measurement technique (all angles in a single image), the angular shape of the upwelling radiance ($L_u(\lambda,\Omega)/L_u(\lambda,0°)$) is a much more accurate parameter. In this paper we compare the angular shape of $L_w(\lambda,\Omega)/L_w(\lambda,0°)$ in the model and measurements. For measurements, $L_w(\lambda,\Omega)/L_w(\lambda,0°)$ was obtained by applying the ratio of $\Re(\Omega)/R(0°)$ (see Gordon [7]) to $L_u(\lambda,\Omega)/L_u(\lambda,0°)$, which was calculated directly from the NuRADS measurements. In the model, $L_w(\lambda,\Omega)/L_w(\lambda,0°)$ was estimated from $R_{rs}(\lambda,\Omega)$ using the IOP-centered approach.

Results of two completely different waters are presented, where the sky was clear without clouds. One was measured in blue water (Mediterranean Sea, AOPEX station 0807125900, Aug. 7, 2004) with the sun at ~30° from zenith; the other was measured in green water (Monterey Bay, Sept. 15, 2006) with a sun angle ~60° from zenith. For the AOPEX station, R_{rs} was derived from upwelling radiance and downwelling irradiance measured from three TriOS radiometers (for example, see Lubac and Loisel [53]). For the Monterey Bay station, R_{rs} was measured at $(30°, 90°)$ with a handheld spectroradiometer [54,55]. The measured R_{rs} of the two stations are presented in Fig. 5. The absorption coefficient at 440 nm (derived from QAA) of the two stations was ~0.025 m^{-1} and 0.9 m^{-1}, while their euphotic zone depths [56] were ~108 m and 7.2 m, respectively, indicating significantly different water environments.

Following the IOP-centered BRDF correction scheme, the absorption and backscattering coefficients were derived first from R_{rs} by incorporating their corresponding model coefficients for ($G_0^w(\Omega)$, $G_1^w(\Omega)$, $G_0^p(\Omega)$, and $G_1^p(\Omega)$). With these IOPs, $R_{rs}(\lambda,0°)$ and $R_{rs}(\lambda,\Omega)$, and the ratio $R_{rs}(\lambda,\Omega)/R_{rs}(\lambda,0°)$ (which equals to $L_w(\lambda,\Omega)/L_w(\lambda,0°)$) were calculated with the angular coefficients developed in Section 3. As examples, Figs. 6 and 7 (blue symbols) compare measured and calculated $L_w(\lambda,\Omega)/L_w(\lambda,0°)$ of selected viewing angles and wavelengths.

For the AOPEX station (Fig. 6), because the sun is at 30° from zenith, the angular variation among $L_w(\lambda,\Omega)/L_w(\lambda,0°)$ is quite narrow (between 0.9 and 1.1) for θ_v within 70°. In this relatively clear water, molecule scattering dominates the scattering processes in the shorter wavelengths ($b_{bw}/b_b \sim 75\%$ at 412 nm), and the distribution of upwelling radiance is more isotropic [1]. In addition, the smaller solar zenith angle limits the contribution of forward scattered photons from the solar beam to $L_w(\lambda,60°,0°)$.

To evaluate the overall performance of the BRDF correction scheme in the remote sensing domain ($\theta_v = 0$–$71°$, $\varphi = 0$–$180°$), as examples, $L_w(\lambda,\theta_S,\theta_v,\varphi)/L_w(\lambda,\theta_S,0°,0°)$ for λ as 412 and 550 nm are presented at the lower panel of Fig. 6, respectively. Statistically, the coefficient of determination (R^2) is 0.86 and 0.77, with averaged δ values of 1.4% and 1.7% for the two wavelengths, respectively.

For comparison, $L_w(\lambda,\Omega)/L_w(\lambda,0°)$ ratios derived from the Chl-based approach [4,5] are also presented (green square in Fig. 6), where Chl concentration was ~0.08 mg/m^3 based on the OC4v4 algorithm [57]. The same $R(\Omega)/R(0°)$ ratios used for the NuRADS data were applied to convert the below-surface radiance ratio to the above-surface radiance ratio. Generally, the results of the two approaches are similar, which is evidenced by the R^2 values (0.89 and 0.84 for 412 nm and 550 nm, respectively) and the δ values (1.4% and 2.2% for 412 nm and 550 nm, respectively). These results imply that for oceanic waters, a consistent BRDF correction could be achieved from both the Chl-based and IOPs-based approaches, but more tests and evaluations with extensive measurements are necessary.

For the measurements made in Monterey Bay, however, a different picture emerges. For the measurements with $\theta_v = 30°$, the $L_w(440,30°,\varphi)/L_w(440,0°,0°)$ ratio is generally around 1.0, except for those where φ is close to 0°, an angle where more

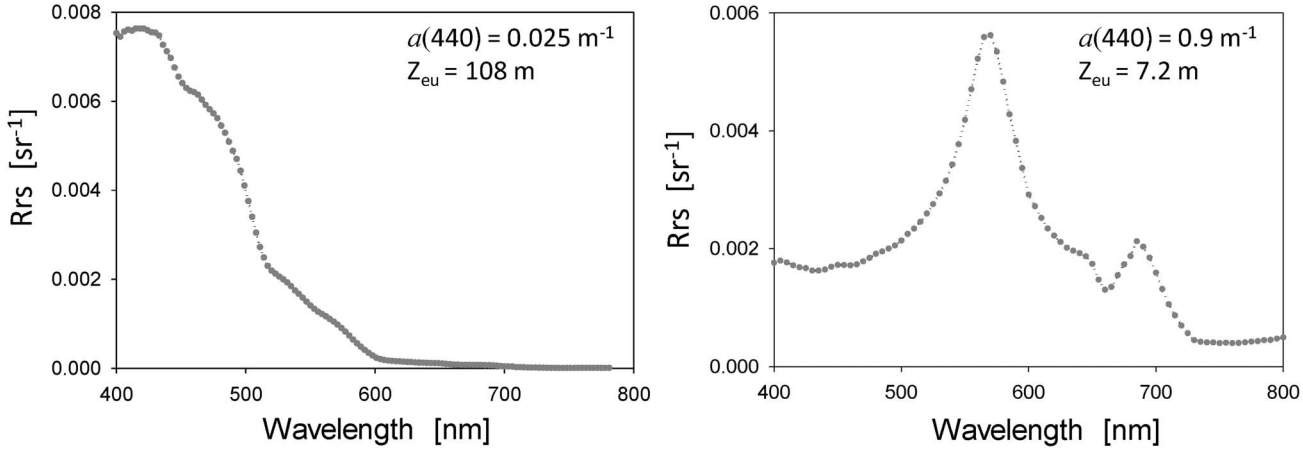

Fig. 5. Remote sensing reflectance of the two sample stations: (left) measured in the Mediterranean Sea, (right) measured in the Monterey Bay.

forward scattered solar photons contribute to L_w. This is significantly pronounced for $\theta_v = 60°$ and φ close to 0° (Fig. 7). Because the sun was at ~60° (~40° below the sea surface), and because particle scattering dominates in this environment ($b_{bw}/b_b \sim 10\%$ at 412 nm), more multiple forward scattered solar photons contribute to $L_w(\lambda, 60°, \varphi \sim 0°)$ than to $L_w(\lambda, 0°, 0°)$, and consequently $L_w(\lambda, 60°, \varphi \sim 0°)/L_w(\lambda, 0°, 0°)$ was as high as 1.7 [58]. Note that, for $\theta_v = 60°$ and $\varphi \sim 90°$, $L_w(\lambda, 60°, \varphi \sim 0°)/L_w(\lambda, 0°, 0°)$ is only around 1.2. For $\theta_v = 60°$ and $\varphi \sim 180°$, however, because it is in the angular range of the instrument self shadow, the measured $L_w(\lambda, 60°, 60°, \varphi \sim 180°)/L_w(\lambda, 60°, 0°, 0°)$ dropped to ~0.80. Instrument self shading [59], however, is minor in the blue spectral region for clear waters [51].

Similarly to Fig. 6, $L_w(\lambda, \theta_S, \theta_v, \varphi)/L_w(\lambda, \theta_S, 0°, 0°)$ for λ as 440 and 550 nm are presented at the lower panel of Fig. 7, respectively. The R^2 values are 0.95 and 0.98, with averaged δ values as 3.5% and 4.1% for the two wavelengths, respectively. Because of instrument self shading, data with φ in the range of 150–180° (the open symbol in Fig. 7) were excluded in the statistical analysis. The Chl value was ~27.7 mg/m^3 (derived empirically from the R_{rs} ratio), which is beyond the Chl range of the Chl-based approach [5], thus no $L_w(\lambda, \theta_S, \theta_v, \varphi)/L_w(\lambda, \theta_S, 0°, 0°)$ ratio was derived from the Chl-based approach for this measurement.

The above results indicate that between the NuRADS measurements and the R_{rs} estimations, the $L_w(\theta_S, \theta_v, \varphi)/L_w(\theta_S, 0°, 0°)$ ratios of both oceanic and coastal waters were very consistent qualitatively and quantitatively and thus validate the IOP-based BRDF correction system, at least for these measurements.

2. *Comparison Using the Wire-Stabilized Environmental Profiling Radiometer and the Ocean Color Component of the Aerosol Robotic Network Data*

Another evaluation was carried out with 63 pairs of water-leaving radiance data determined from almost simultaneous above- and in-water radiometric measurements (i.e., collected within 15 minutes from each other) and performed at the Acqua Alta Oceanographic Tower (AAOT) in the northern Adriatic Sea during clear sky conditions. These measurements were made from June 2002 to November 2008 in a variety of observation conditions indicated by sun zenith θ_S varying in the range of ~23–70° and chlorophyll-a concentration (as quantified through high precision liquid chromatography) in the range of ~0.2–3.3 mg/m^3.

Above-water data were produced with modified CE-318 (CIMEL, France) radiometers [60] integrated in the Ocean Color component of the Aerosol Robotic Network (AERONET-OC). These water-leaving

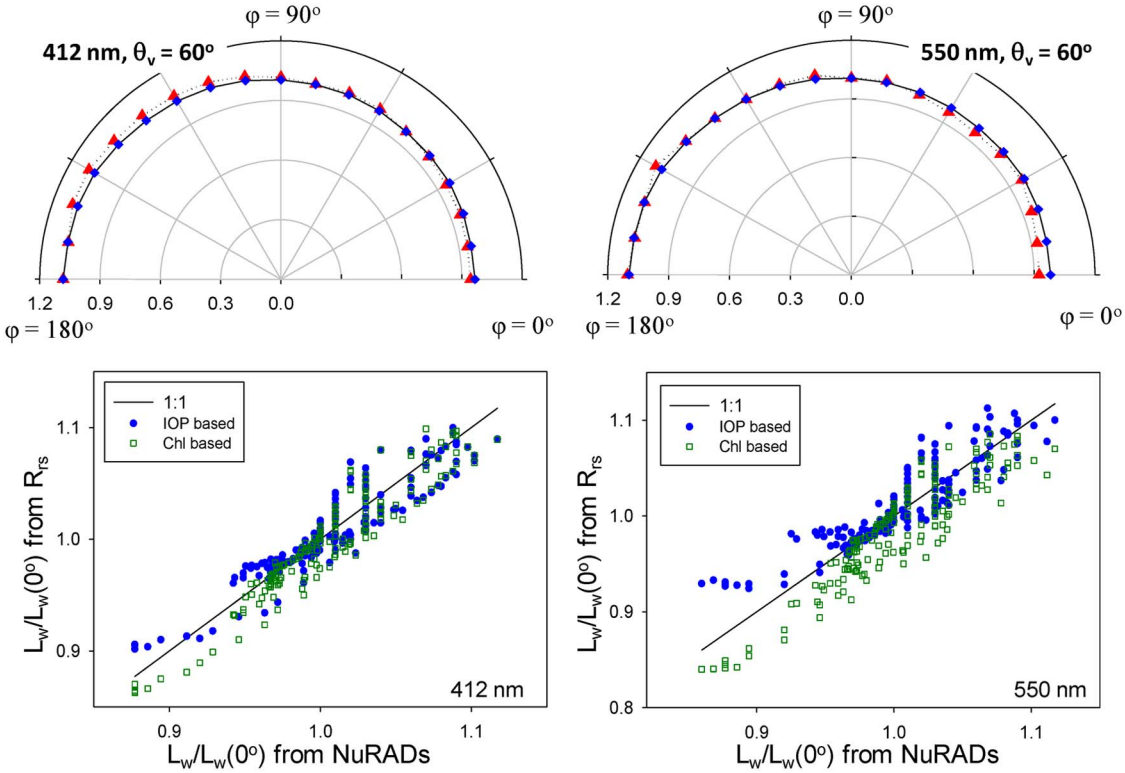

Fig. 6. (Color online) (Top panel) Comparison between measured and derived $L_w(\lambda, \Omega)/L_w(\lambda, 0°)$ for selected wavelength and viewing angle of measurements made in the Mediterranean Sea. Red triangle represents measurements from the NuRADS; blue diamond represents values calculated from R_{rs} (IOPs-centered approach). (Bottom panel) Comparison between measured and derived $L_w(\lambda, \Omega)/L_w(\lambda, 0°)$ for Ω in the remote sensing domain (blue circle, IOPs-centered approach; green square, Chl-centered approach).

radiance data, $L_w(\lambda,\theta_S,40°,90°)$, were determined at a 40° viewing angle and 90° relative azimuth with respect to the sun [61]. Water-leaving radiance data from in-water radiometric measurements, $L_w(\lambda,\theta_S,0°,0°)$, were determined from subsurface upwelling radiance $L_u(\lambda,\theta_S,0°,0°)$ extrapolated from near-surface nadir-view measurements performed with the Wire-Stabilized Environmental Profiling Radiometer (WiSPER) system [62]. Spectral differences between the two datasets were minimized applying a band-shift correction relying on site-specific, bio-optical algorithms [63].

$R_{rs}(\lambda,\theta_S,40°,90°)$ was calculated for each set of $L_w(\lambda,\theta_S,40°,90°)$ using theoretical determinations of $E_d(0^+,\lambda,\theta_S)$ for clear sky conditions [60], and then fed to the QAA (Section 4) to derive a and b_b values. With these a and b_b values, and the values of $(G_0^w(\Omega)$, $G_1^w(\Omega)$, $G_0^p(\Omega)$, and $G_1^p(\Omega))$ for $\Omega=(\theta_S,0°,0°)$ and $\Omega=(\theta_S,40°,90°)$, $R_{rs}(\lambda,\theta_S,0°,0°)/R_{rs}(\lambda,\theta_S,40°,90°)$ were calculated for each $L_w(\lambda,\theta_S,40°,90°)$, and then $L_w(\lambda,\theta_S,0°,0°)$ were determined as the product of $R_{rs}(\lambda,\theta_S,0°,0°)/R_{rs}(\lambda,\theta_S,40°,90°)$ and $L_w(\lambda,\theta_S,40°,90°)$.

The $L_w(\lambda,\theta_S,0°,0°)$ calculated from the AERONET-OC $L_w(\lambda,\theta_S,40°,90°)$ are compared with the WiSPER $L_w(\lambda,\theta_S,0°,0°)$, and results are presented in Fig. 8 (blue symbols) for wavelengths of 411, 443, 490, and 555 nm. The averages of signed percent differences (determined to quantify biases between compared vales) are 1.9%, −0.8%, −3.2%, and −3.1% at the four wavelengths, respectively. The averages of the absolute of percent differences (determined to quantify scattering of compared values) are 7.8%, 6.9%, 8.0%, and 6.8%. If the BRDF correction is conducted with the Chl-based approach (green symbols in Fig. 8, where Chl was estimated with a regional algorithm [64]), the averages of signed percent differences are 2.3%, −0.0%, −1.5%, and −1.6%; and the averages of the absolute of the percent differences are 8.2%, 7.4%, 8.4%, and 7.1%, respectively, similar as that from the IOP-based approach. This is likely due to the relatively small angular effects between $(40°,90°)$ and $(0°,0°)$ [1,5], as without a BRDF correction, the average of the signed percent differences was approximately −2.2%, −5.3%, −8.2%, and −8.2%, respectively, while the absolute of percent differences are ∼8% at all wavelengths. The above comparisons indicate that both the IOP-based and Chl-based BRDF corrections did reduce bias but not appreciably the scattering among compared data when considering $L_w(\lambda,\theta_S,0°,0°)$ from measured $L_w(\lambda,\theta_S,40°,90°)$. The latter insignificant decrease in the average absolute percent differences is explained, at least in part, by uncertainties characterizing measurements of water-leaving radiance through two fully independent instruments and methods.

3. *Sensitivity of the IOP-Based Approach on the IOPs Retrieval*

Because of various assumptions, approximations, and empiricism, a full set of IOPs cannot be retrieved precisely from the measurement of R_{rs} (or L_w). To

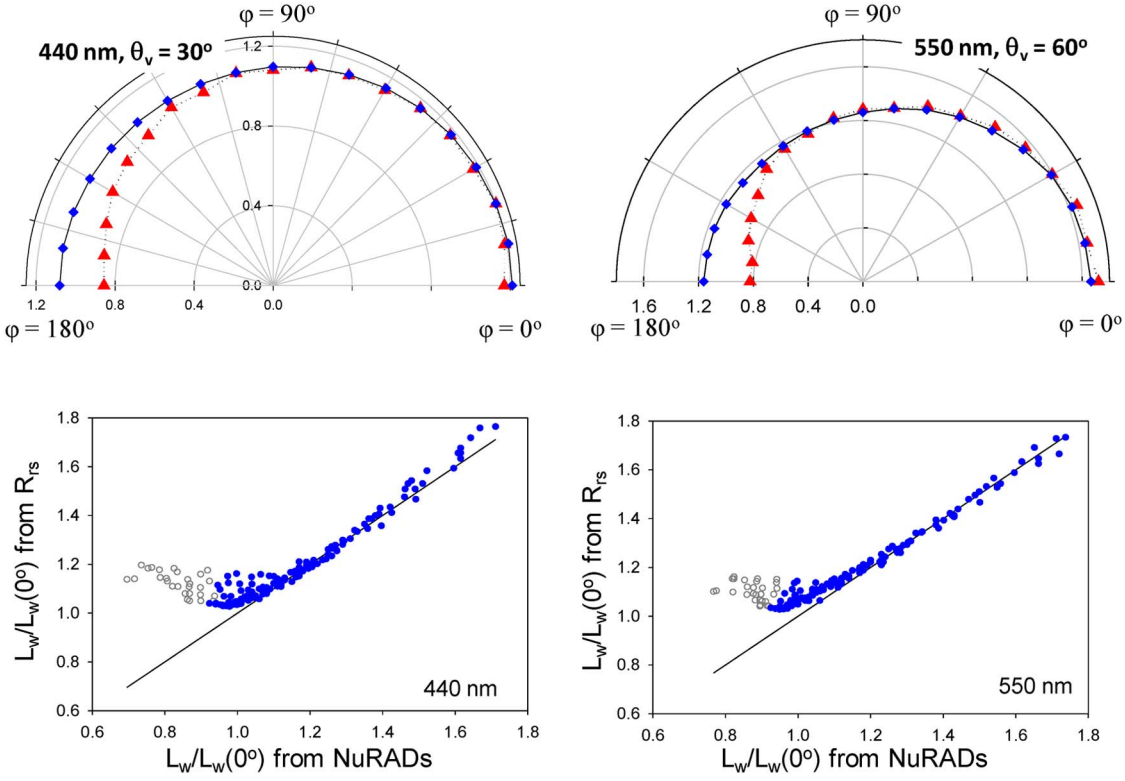

Fig. 7. (Color online) As Fig. 5, for measurements made in the Monterey Bay.

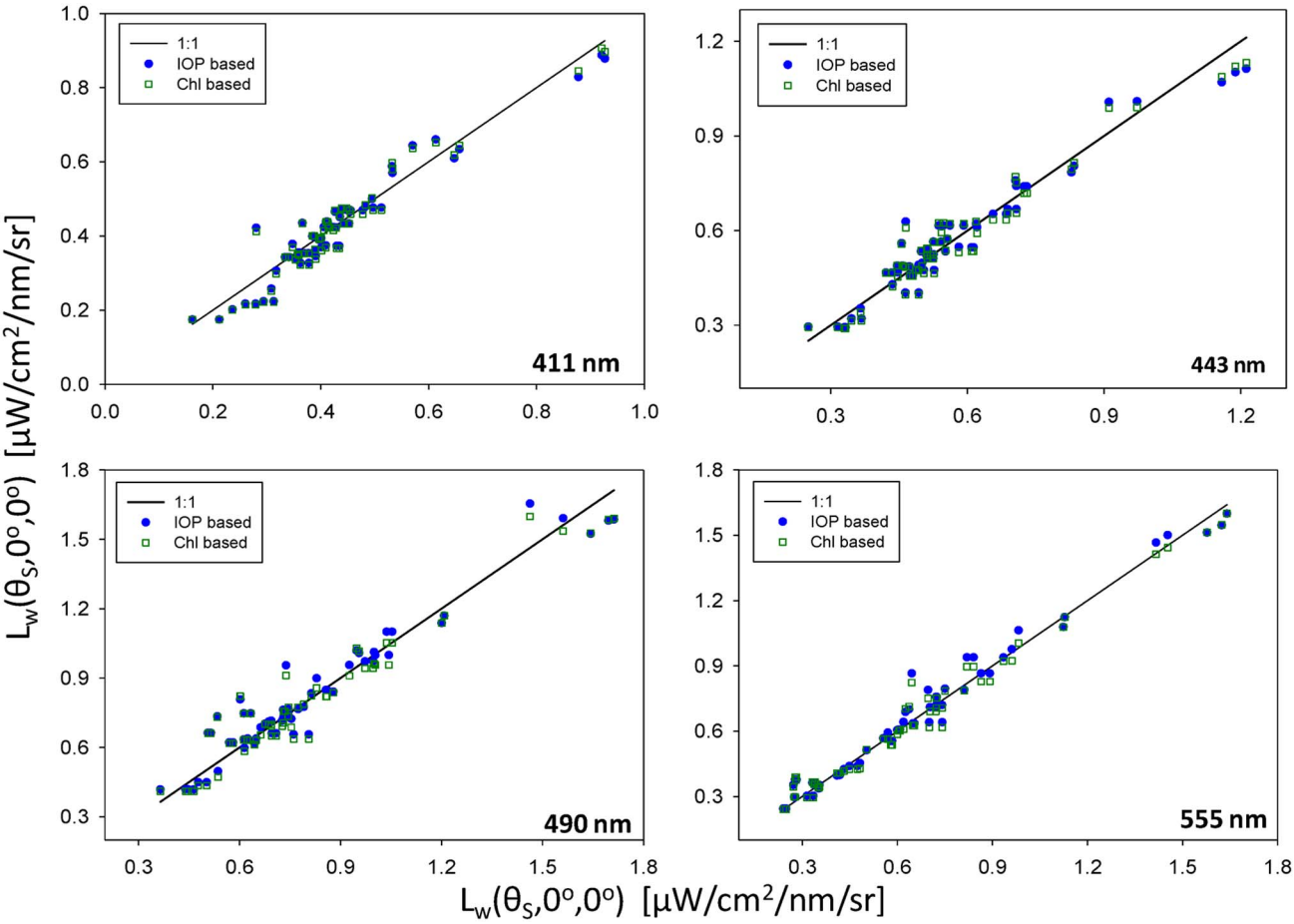

Fig. 8. (Color online) Comparison between measured and derived $L_w(\lambda,\theta_S,0°,0°)$ for measurements made at the AAOT. The x axis represents $L_w(\lambda,\theta_S,0°,0°)$ measured by the WiSPER, while the y axis represents $L_w(\lambda,\theta_S,0°,0°)$ calculated from $L_w(\lambda,\theta_S,40°,90°)$ which was measured by a CE-318 radiometer (blue circle, IOPs-centered approach; green square, Chl-centered approach).

understand the impact of IOP's uncertainties on the IOP-based BRDF correction, for example, Fig. 9 presents the change of $L_w(\theta_S,\theta_v,\varphi)/L_w(\theta_S,0°,0°)$ corresponding to the change of $a(\lambda_0)$ for the two sample measurements in Subsection 5.B.1. We show this because $a(\lambda_0)$ is a key quantity in the QAA inversion scheme for the sequential calculation of other optical properties. Errors or uncertainties of the other derived properties are highly dependent on the accuracy of $a(\lambda_0)$ but not uniformly for different waters [47].

For the measurements made in the Mediterranean Sea (blue water), a $\pm 10\%$ uncertainty of $a(550)$ was used for the sensitivity evaluation (Fig. 9, top panel), while a $\pm 20\%$ uncertainty of $a(550)$ was used for the Monterey Bay water (Fig. 9, bottom panel). For the two waters and the two wavelengths (412 and 550 nm), it is found that the impact of 10% or 20% uncertainty of $a(\lambda_0)$ on the ratio of $L_w(\theta_S,\theta_v,\varphi)/L_w(\theta_S,0°,0°)$ is limited. Generally, an increase of $a(\lambda_0)$ will increase the ratio of $L_w(\theta_S,\theta_v,\varphi)/L_w(\theta_S,0°,0°)$; while a decrease of $a(\lambda_0)$ will decrease the ratio of $L_w(\theta_S,\theta_v,\varphi)/L_w(\theta_S,0°,0°)$ in similar magnitude. For the blue water, a 10% increase of $a(550)$ resulted in 2.4%, 2.7%, 3.2%, and 3.8% increase of $L_w(\theta_S,\theta_v,\varphi)/L_w(\theta_S,0°,0°)$ for wavelengths of 412, 440, 490, and 550 nm, respectively, which are smaller or equivalent to the measurement uncertainties [65]. For the green water, although values of $a(550)$ were altered by 20%, the resulted impact on the $L_w(\theta_S,\theta_v,\varphi)/L_w(\theta_S,0°,0°)$ ratio is about or less than 1% for 412, 440, 490, and 550 nm, respectively.

The limited sensitivity of the $L_w(\theta_S,\theta_v,\varphi)/L_w(\theta_S,0°,0°)$ ratio to the uncertainty of the IOPs is because (1) R_{rs} is generally a function of $b_b/(a+b_b)$ (e.g., Eqs. (6) and (14)). When we use an R_{rs} model to analytically derive a and b_b, although the derived a or b_b values may be inaccurate in some degree but the retrieved $b_b/(a+b_b)$ maintains the same (e.g., the QAA scheme). (2) The angular variation of $R_{rs}(\theta_S,\theta_v,\varphi)$ is primarily governed by the $G(\Omega)$ coefficients (Eq. (14)), which is determined for given particle phase functions.

The larger uncertainty in the $L_w(\theta_S,\theta_v,\varphi)/L_w(\theta_S,0°,0°)$ ratio of the blue water (comparing to that of the green water) is due to a lower contribution of particle backscattering to the upwelling radiance with respect to molecular backscattering (b_{bp}/b_b was $\sim 25\%$ at 412 nm). As a result, the relative weighting

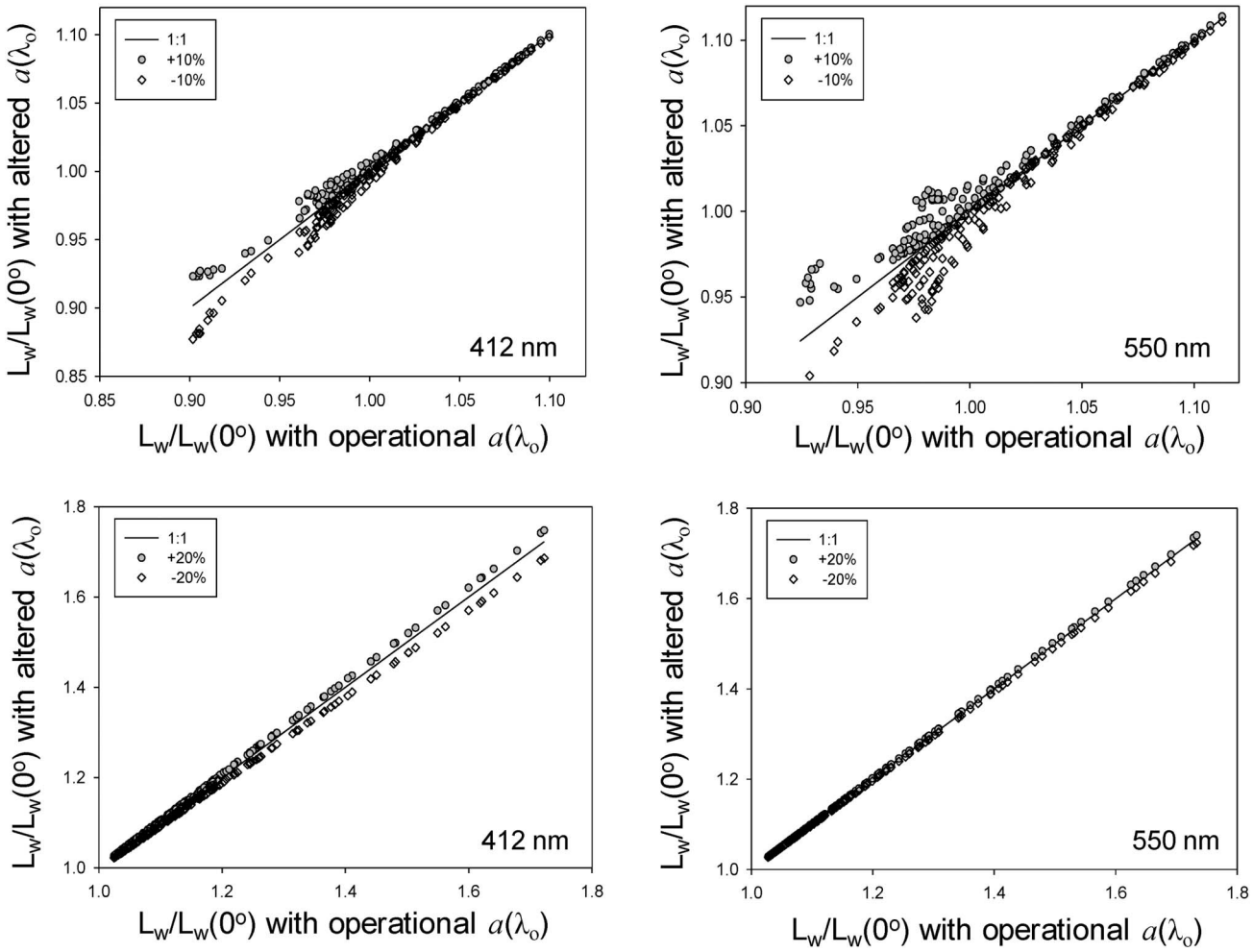

Fig. 9. Scatter plot of $L_w(\lambda,\Omega)/L_w(\lambda,0^\circ)$ for different values of $a(\lambda_0)$. The x axis represents the $L_w(\lambda,\Omega)/L_w(\lambda,0^\circ)$ ratio derived with $a(550)$ in the current QAA scheme; the y-axis represents the $L_w(\lambda,\Omega)/L_w(\lambda,0^\circ)$ ratio derived after altering the estimated $a(550)$. Top panel, the blue water in the Mediterranean Sea, $a(550)$ was altered by $\pm 10\%$; bottom panel, the green water in the Monterey Bay, $a(550)$ was altered by $\pm 20\%$.

of molecular scattering will be sensitive to the derived b_{bp} value. Because molecular scattering and particle scattering have quite different angular shapes, uncertainty in the b_{bp} value (resulted from uncertainty in $a(\lambda_0)$, for instance) will thus affect the ratio of $L_w(\theta_S,\theta_v,\varphi)/L_w(\theta_S,0^\circ,0^\circ)$, which is highly dependent on the shape of the VSF. For the green water, however, contribution from molecular backscattering was $\sim 10\%$ of the total backscattering, thus the phase function shape of molecular scattering had a small impact on the shape of the VSF, and a smaller variation in the $L_w(\theta_S,\theta_v,\varphi)/L_w(\theta_S,0^\circ,0^\circ)$ ratio due to the uncertainty of $a(\lambda_0)$ was found. These results and analyses indicate slightly larger uncertainties in the BRDF correction in oceanic waters, but this uncertainty will generally be within measurement uncertainties as long as the particle phase function is well defined.

6. Summary

A system centered on IOPs has been developed for the correction of angular effects in water-leaving radiance of optically-deep waters. This system is not restricted to Case 1 waters and focuses on the derivation of the total absorption and backscattering coefficients from the measured, angular, and spectral remote-sensing reflectance. The system is also applicable to multispectral sensors (e.g., SeaWiFS, MODIS, and MERIS) and hyperspectral sensors. The system was applied to both a numerically simulated dataset and a field measured dataset to test and evaluate its performance, and it is found that application of the system produced adequate estimates of the zenith radiance from that measured at other angles. These results suggest that the system could be applied to ocean color remote sensing to (1) derive IOPs of both oceanic and coastal waters from the angular remote sensing reflectance (or angular water-leaving radiance), and (2) generate normalized water-leaving radiance from the derived IOPs for calibration and validation activities.

However, it is necessary to keep in mind that the accuracy of all analytical models (including the model developed and used here) describing the remote

sensing reflectance is limited by the accuracy of the numerical representation of the radiative transfer in natural waters. More importantly, all models explicitly or inexplicitly include an assumption about the angular shape of the particle scattering function. This angular shape plays an important role in forming the angular distribution of the upwelling radiance, while at the same time it cannot be accurately determined yet from a remote sensing measurement. Because the exact angular shape of particle phase function is not known *a priori* for a given water body in remote sensing, and the model accuracy is no better than the accuracy of the numerical simulations, correction of the angular variation of water-leaving radiance based on the IOPs or other properties is, to the best, a first order improvement.

Financial support from the Naval Research Laboratory (Lee, Arnone, Weidemann), the National Aeronautics and Space Administration (NASA) Ocean Biology and Biogeochemistry (Lee, Voss) and the Water and Energy Cycle (Lee) Programs, the Korea Ocean Research and Development Institute (Lee), and the National Key Basic Research Program of China (973 Program, grant 2007CB714407, Du) are greatly appreciated. The authors also wish to thank the NASA AERONET team for the continuous effort in processing and quality assuring AERONET-OC data. The AOPEX cruise is part of the BOUSSOLE project, which is funded by the CNRS, the Institut National des Sciences de l'Univers, the Centre National d'Etudes Spatiales, the European Space Agency, and the NASA through a Letter of Agreement with the Université Pierre et Marie Curie. Shiptime on the Suroît R/V was funded by the Institut français de recherche pour l'exploitation de la mer. We are grateful for the comments and suggestions from two anonymous reviewers.

References

1. A. Morel and B. Gentili, "Diffuse reflectance of oceanic waters (2): bi-directional aspects," Appl. Opt. **32**, 6864–6879 (1993).
2. H. R. Gordon and D. K. Clark, "Clear water radiances for atmospheric correction of coastal zone color scanner imagery," Appl. Opt. **20**, 4175–4180 (1981).
3. H. R. Gordon and K. J. Voss, "Normalized water-leaving radiance," Tech. Rep. (National Aeronautics and Space Administration, 1999).
4. A. Morel and B. Gentili, "Diffuse reflectance of oceanic waters, III, implications of bi-directionality for the remote sensing problem," Appl. Opt. **35**, 4850–4862 (1996).
5. A. Morel, D. Antoine, and B. Gentili, "Bidirectional reflectance of oceanic waters: accounting for Raman emission and varying particle scattering phase function," Appl. Opt. **41**, 6289–6306 (2002).
6. A. Morel and L. Prieur, "Analysis of variations in ocean color," Limnol. Oceanog. **22**, 709–722 (1977).
7. H. R. Gordon, "Normalized water-leaving radiance: revisiting the influence of surface roughness," Appl. Opt. **44**, 241–248 (2005).
8. A. Morel and B. Gentili, "Diffuse reflectance of oceanic waters: its dependence on sun angle as influenced by the molecular scattering contribution," Appl. Opt. **30**, 4427–4438 (1991).
9. H. R. Gordon, "Atmospheric correction of ocean color imagery in the Earth observing system era," J. Geophys. Res. **102**, 17081–17106 (1997).
10. H. R. Gordon and A. Morel, *Remote Assessment of Ocean Color for Interpretation of Satellite Visible Imagery: A Review* (Springer-Verlag, 1983), p. 44.
11. International Ocean Colour Coordinating Group, "Remote sensing of ocean colour in coastal, and other optically-complex, waters," in Reports of the International Ocean-Colour Coordinating Group, No. 3, S. Sathyendranath, ed. (International Ocean Colour Coordinating Group, Dartmouth, Canada, 2000).
12. A. Morel and S. Maritorena, "Bio-optical properties of oceanic waters: a reappraisal," J. Geophys. Res. **106**, 7163–7180 (2001).
13. K. J. Voss, A. Morel, and D. Antoine, "Detailed validation of the bidirectional effect in various case 1 waters for application to ocean color imagery," Biogeosciences **4**, 781–789 (2007).
14. A. Morel, "Are the empirical relationships describing the bio-optical properties of case 1 waters consistent and internally compatible?," J. Geophys. Res. **114**, C01016 (2009).
15. Z. P. Lee and C. Hu, "Global distribution of case-1 waters: an analysis from SeaWiFS measurements," Remote Sens. Environ. **101**, 270–276 (2006).
16. C. D. Mobley, H. Zhang, and K. J. Voss, "Effects of optically shallow bottoms on upwelling radiances: bidirectional reflectance distribution function effects," Limnol. Oceanog. **48**, 337–345 (2003).
17. R. H. Stavn and A. D. Weidemann, "Optical modeling of clear ocean light fields: Raman scattering effects," Appl. Opt. **27**, 4002–4011 (1988).
18. C. Hu and K. J. Voss, "In situ measurements of Raman scattering in clear ocean water," Appl. Opt. **36**, 6962–6967 (1997).
19. H. R. Gordon, K. J. Voss, and K. A. Kilpatrick, "Angular distribution of fluorescence from phytoplankton," Limnol. Oceanog. **38**, 1582–1586 (1993).
20. C. D. Mobley, *Light and Water: Radiative Transfer in Natural Waters* (Academic, 1994).
21. J. R. V. Zaneveld, "Remote sensed reflectance and its dependence on vertical structure: a theoretical derivation," Appl. Opt. **21**, 4146–4150 (1982).
22. J. R. V. Zaneveld, "A theoretical derivation of the dependence of the remotely sensed reflectance of the ocean on the inherent optical properties," J. Geophys. Res. **100**, 13135–13142 (1995).
23. H. R. Gordon, O. B. Brown, and M. M. Jacobs, "Computed relationship between the inherent and apparent optical properties of a flat homogeneous ocean," Appl. Opt. **14**, 417–427 (1975).
24. H. R. Gordon, O. B. Brown, R. H. Evans, J. W. Brown, R. C. Smith, K. S. Baker, and D. K. Clark, "A semianalytic radiance model of ocean color," J. Geophys. Res. **93**, 10909–10924 (1988).
25. H. R. Gordon, "Modeling and simulating radiative transfer in the ocean," in *Ocean Optics*, R. W. Spinrad, K. L. Carder, and M. J. Perry, eds. (Oxford University, 1994).
26. N. K. Hojerslev, "Analytic remote-sensing optical algorithms requiring simple and practical field parameter inputs," Appl. Opt. **40**, 4870–4874 (2001).
27. T. Hirata, N. Hardman-Mountford, J. Aiken, and J. Fishwick, "Relationship between the distribution function of ocean nadir radiance and inherent optical properties for oceanic waters," Appl. Opt. **48**, 3130–3139 (2009).
28. C. D. Mobley, L. K. Sundman, and E. Boss, "Phase function effects on oceanic light fields," Appl. Opt. **41**, 1035–1050 (2002).
29. T. J. Petzold, "Volume scattering functions for selected natural waters," Scripps Inst. Oceanog. 72–78 (1972).

30. M. E. Lee and M. R. Lewis, "A new method for the measurement of the optical volume scattering function in the upper ocean," J. Atmos. Ocean. Technol. **20**, 563–571 (2003).
31. J. M. Sullivan and M. S. Twardowski, "Angular shape of the oceanic particulate volume scattering function in the backward direction," Appl. Opt. **48**, 6811–6819 (2009).
32. J. T. O. Kirk, "Dependence of relationship between inherent and apparent optical properties of water on solar altitude," Limnol. Oceanog. **29**, 350–356 (1984).
33. H. R. Gordon, "Can the Lambert-Beer law be applied to the diffuse attenuation coefficient of ocean water?," Limnol. Oceanog. **34**, 1389–1409 (1989).
34. E. Åas, "Two stream irradiance model for deep waters," Appl. Opt. **26**, 2095–2101 (1987).
35. Z. P. Lee, K. P. Du, and R. Arnone, "A model for the diffuse attenuation coefficient of downwelling irradiance," J. Geophys. Res. **110**, C02016, (2005).
36. A. Albert and C. D. Mobley, "An analytical model for subsurface irradiance and remote sensing reflectance in deep and shallow case-2 waters," Opt. Express **11**, 2873–2890 (2003).
37. S. Sathyendranath and T. Platt, "Analytic model of ocean color," Appl. Opt. **36**, 2620–2629 (1997).
38. Z. P. Lee, K. L. Carder, S. K. Hawes, R. G. Steward, T. G. Peacock, and C. O. Davis, "A model for interpretation of hyperspectral remote sensing reflectance," Appl. Opt. **33**, 5721–5732 (1994).
39. Z. P. Lee, K. L. Carder, and K. P. Du, "Effects of molecular and particle scatterings on model parameters for remote-sensing reflectance," Appl. Opt. **43**, 4957–4964 (2004).
40. Y.-J. Park and K. Ruddick, "Model of remote-sensing reflectance including bidirectional effects for case 1 and case 2 waters," Appl. Opt. **44**, 1236–1249 (2005).
41. H. J. V. D. Woerd and R. Pasterkamp, "HYDROPT: a fast and flexible method to retrieve chlorophyll-a from multispectral satellite observations of optically complex coastal waters," Remote Sens. Environ. **112**, 1795–1807 (2008).
42. Z. P. Lee, K. L. Carder, C. D. Mobley, R. G. Steward, and J. S. Patch, "Hyperspectral remote sensing for shallow waters. 1. A semianalytical model," Appl. Opt. **37**, 6329–6338 (1998).
43. International Ocean Colour Coordinating Group, "Remote sensing of inherent optical properties: fundamentals, tests of algorithms, and applications," in Reports of the International Ocean-Colour Coordinating Group, No. 5, Z.-P. Lee, ed. (International Ocean Colour Coordinating Group, Dartmouth, Canada, 2006), p. 126.
44. G. R. Fournier and J. L. Forand, "Analytic phase function for ocean water," in *Ocean Optics XII*, J. S. Jaffe, eds. (SPIE, 1994), pp. 194–201
45. C. D. Mobley, *Hydrolight 3.0 Users' Guide* (SRI, 1995).
46. Z. P. Lee, K. L. Carder, and R. Arnone, "Deriving inherent optical properties from water color: a multi-band quasi-analytical algorithm for optically deep waters," Appl. Opt. **41**, 5755–5772 (2002).
47. Z.-P. Lee, R. Arnone, C. Hu, P. J. Werdell, and B. Lubac, "Uncertainties of optical parameters and their propagations in an analytical ocean color inversion algorithm," Appl. Opt. **49**, 369–381 (2010).
48. Z. P. Lee, K. L. Carder, T. G. Peacock, C. O. Davis, and J. L. Mueller, "Method to derive ocean absorption coefficients from remote-sensing reflectance," Appl. Opt. **35**, 453–462 (1996).
49. S. Maritorena, D. A. Siegel, and A. R. Peterson, "Optimization of a semianalytical ocean color model for global-scale applications," Appl. Opt. **41**, 2705–2714 (2002).
50. E. Devred, S. Sathyendranath, and T. Platt, "Inversion based on a semi-analytical reflectance model," in *Remote Sensing of Inherent Optical Properties: Fundamentals, Tests of Algorithms and Applications*, Z.-P. Lee, ed. (GKSS, 2006), p. 87–94.
51. K. J. Voss and A. L. Chapin, "Upwelling radiance distribution camera system, NURADS," Opt. Express **13**, 4250–4262 (2005).
52. K. J. Voss and N. Souaidia, "POLRADS: polarization radiance distribution measurement system," Opt. Express **18**, 19672–19680 (2010).
53. B. Lubac and H. Loisel, "Variability and classification of remote sensing reflectance spectra in the eastern English Channel and southern North Sea," Remote Sens. Environ. **110**, 45–58 (2007).
54. K. L. Carder and R. G. Steward, "A remote-sensing reflectance model of a red tide dinoflagellate off West Florida," Limnol. Oceanogr. **30**, 286–298 (1985).
55. Z.-P. Lee, Y.-H. Ahn, C. Mobley, and R. Arnone, "Removal of surface-reflected light for the measurement of remote-sensing reflectance from an above-surface platform," Opt. Express **18**, 26313–26342 (2010).
56. Z. P. Lee, A. Weidemann, J. Kindle, R. Arnone, K. L. Carder, and C. Davis, "Euphotic zone depth: its derivation and implication to ocean-color remote sensing," J. Geophys. Res. **112**, C03009 (2007).
57. J. E. O'Reilly S. Maritorena, D. Siegel, M. C. O'Brien, D. Toole, B. G. Mitchell, M. Kahru, F. P. Chavez, P. Strutton, G. Cota, S. B. Hooker, C. R. McClain, K. L. Carder, F. Muller-Karger, L. Harding, A. Magnuson, D. Phinney, G. F. Moore, J. Aiken, K. R. Arrigo, R. Letelier, andM. Culver, "SeaWiFS postlaunch calibration and validation analyses, part 3," in *SeaWiFS Postlaunch Technical Report Series*, S. B. Hooker and E. R. Firestone, eds. (NASA, 2000), p. 58.
58. H. Loisel and A. Morel, "Non-isotropy of the upward radiance field in typical coastal (Case 2) waters," Int. J. Remote Sens. **22**, 275–295 (2001).
59. H. R. Gordon and K. Ding, "Self-shading of in-water optical instruments," Limnol. Oceanog. **37**, 491–500 (1992).
60. G. Zibordi, F. Mélin, S. B. Hooker, D. D'Alimonte, and B. Holben, "An autonomous above-water system for the validation of ocean color radiance data," IEEE Trans. Geosci. Remote Sens. **43**, 401–415 (2004).
61. G. Zibordi, B. Holben, I. Slutsker, D. Giles, D. D'Alimonte, F. Melin, J.-F. Berthon, D. Vandemark, H. Feng, G. Schuster, B. E. Fabbri, S. Kaitala, and J. Seppala, "AERONET-OC: a network for the validation of ocean color primary products," J. Atmos. Ocean. Technol. **26**, 1634–1651 (2009).
62. G. Zibordi, D. D'Alimonte, and J. F. Berthon, "An evaluation of depth resolution requirements for optical profiling in coastal waters," J. Atmos. Ocean. Technol. **21**, 1059–1073 (2004).
63. G. Zibordi, J.-F. Berthon, F. Mélin, D. D'Alimonte, and S. Kaitala, "Validation of satellite ocean color primary products at optically complex coastal sites: Northern Adriatic Sea, Northern Baltic Proper and Gulf of Finland," Remote Sens. Environ. **113**, 2574–2591 (2009).
64. J.-F. Berthon and G. Zibordi, "Bio-optical relationships for the northern Adriatic Sea," Int. J. Remote Sens. **25**, 1527–1532 (2004).
65. G. Zibordi, B. Holben, S. B. Hooker, F. Mélin, J.-F. Berthon, and I. Slutsker, "A network for standardized ocean color validation measurements," EOS Trans. AGU **87**, 297–298 (2006).